PAPER • OPEN ACCESS

Plasma radiation behavior approaching high-radiation scenarios in W7-X

To cite this article: D. Zhang *et al* 2021 *Nucl. Fusion* **61** 126002

OPEN ACCESS
IOP Publishing | International Atomic Energy Agency Nuclear Fusion
Nucl. Fusion 61 (2021) 126002 (12pp) https://doi.org/10.1088/1741-4326/ac2b75

Plasma radiation behavior approaching high-radiation scenarios in W7-X

D. Zhang*, R. Burhenn, Y. Feng, R. König, B. Buttenschön, C.D. Beidler, P. Hacker, F. Reimold, H. Thomsen, R. Laube, T. Klinger, L. Giannone[1], F. Penzel[1], A. Pavone, M. Krychowiak, M. Beurskens, S. Bozhenkov, J.K. Brunner, F. Effenberg[2], G. Fuchert, Y. Gao, J. Geiger, M. Hirsch, U. Höfel, M. Jakubowski, J. Knauer, S. Kwak, H.P. Laqua, H. Niemann, M. Otte, T. Sunn Pedersen, E. Pasch, N. Pablant[2], K. Rahbarnia, J. Svensson, B. Blackwell[3], P. Drews[4], M. Endler, L. Rudischhauser, E. Wang[4], G. Weir, V. Winters and the W7-X Team[a]

Max-Planck-Institut für Plasmaphysik, D-17491 Greifswald, Germany
[1] Max-Planck-Institut für Plasmaphysik, Garching, Germany
[2] Princeton Plasma Physics Laboratory, Princeton, NJ, United States of America
[3] Australian National University, Canberra, Australia
[4] Institut für Energie und Klimaforschung - Plasmaphysik, Jülich, Germany

E-mail: daihong.zhang@ipp.mpg.de

Received 8 June 2021, revised 25 August 2021
Accepted for publication 29 September 2021
Published 25 October 2021

Abstract

The W7-X stellarator has so far performed experiments under both limiter and divertor conditions. The plasma is mostly generated by ECR-heating with powers up to 6.5 MW, and the plasma density is usually limited by the radiation losses from low-Z impurities (such as carbon and oxygen) released mainly from the graphite targets. The present work first summarizes the radiation loss fractions f_{rad} achieved in quasi-stationary hydrogen plasmas in both operational phases, and then shows how impurity radiation behaves differently with the two different boundary conditions as the plasma density increases. The divertor operation is emphasized and some beneficial effects (with respect to impurity radiation) are highlighted: (1) intensive radiation is located at the edge ($r/a > 0.8$) even at high radiation loss fractions, (2) the plasma remains stable up to f_{rad} approaching unity, (3) the reduction in the stored energy is about 10% for high f_{rad} scenarios. Moreover, effects of wall boronisation on impurity radiation profiles are also presented.

Keywords: plasma radiation, W7-X stellarator, the island divertor vs. limiter configuration, high-radiation scenarios, plasma detachment

(Some figures may appear in colour only in the online journal)

---

[*] Author to whom any correspondence should be addressed.

[a] See Klinger *et al* 2019 (https://doi.org/10.1088/1741-4326/ab03a7) for the W7-X Team

1. Introduction

W7-X is an optimized quasi-isodynamic stellarator [1] with non-planar superconducting coils. It is designed for long-pulse steady-state plasma operation with the goal to bring the optimized stellarator to reactor maturity. Demonstration of a reactor-relevant island divertor concept is one of its main scientific objectives [2–4]. The W7-X stellarator has so far performed experiments under both limiter [5, 6] and divertor conditions [7, 8]. While in the first case smooth flux surfaces are cut by five local limiters producing a plasma edge free of low-order resonances [9, 10], in the second case a low-order magnetic island chain (e.g. with $\iota = n/m = 5/6, 5/5$, and $5/4$) is cut by ten sophisticated divertor units [11]. Both the limiters and the divertor targets are made of graphite tiles. This raises interesting questions of how and to what extent the different plasma boundary conditions affect the impurity radiation and thus the plasma performance, in particular through radiation-driven thermal instability. To date, publications on the thermal energy dissipation capability of the island divertor in W7-X have reported that the power incident on the targets can be dissipated by line radiation from low-Z impurities (mainly carbon and oxygen) without relatively strong deterioration of the core plasma performance. These stable high-density, high-radiation regimes (with plasma detachment) were achieved in the divertor operational phases before and after wall boronisation in 2017 (OP1.2a) and 2018 (OP1.2b), respectively [12, 13]. A key question raised is: how differently does the impurity radiation behave in the limiter and divertor configurations, especially as plasma density increases for dedicated high-performance? This is the main objective addressed in this paper.

This paper is organized as follows: section 2 describes the general observation regarding the radiation loss fraction in the W7-X plasma; section 3 demonstrates the beneficial effects of the island divertor compared to the limiter configuration; section 4 compares the radiation profiles with respect to the plasma boundary conditions. Section 5 provides a discussion of the underlying physics together with a summary.

2. General observations

Figure 1 (top) shows the data points of the radiation loss fraction $f_{\rm rad}$ as a function of the average plasma density in divertor configuration ('standard' with $n/m = 5/5$). It is defined by $f_{\rm rad} = P_{\rm rad}/P_{\rm heat}$, where $P_{\rm rad}$ is the total radiated power of the plasma and $P_{\rm heat}$ the effective heating power. They were recorded from quasi-stationary states of the hydrogen plasma with electron cyclotron resonance heating (ECRH) [14] with powers (in different colors) up to 6.5 MW. Experiments with pellet injection are not included. $P_{\rm rad}$ is obtained by linearly scaling the radiated power measured in the viewing volume of a horizontal bolometer camera [15] (whose lines of sight have good coverage over the triangular plasma cross section under study) to the total plasma volume [12]. It is clearly seen that the data points fall into two branches labeled OP1.2a (in 2017 before boronisation) and OP1.2b (in 2018 after boronisation), respectively. The dashed and dotted lines are fits to the data at low and high heating power based on the functions $y = kx^2$, with $k = 10$–30 for OP1.2a and 0.7–2.5 for OP1.2b, respectively. The k-value reflects how fast the impurity radiation increases with plasma density. Additionally, a shaded area shows the parameter range in the limiter configuration (OP1.1) and the data collected for varied $P_{\rm heat}$ in the later phase of OP1.1 (in 2016) are shown in figure 1 (bottom) (for more details, see [16]), where the dashed lines are only to guide the eye.

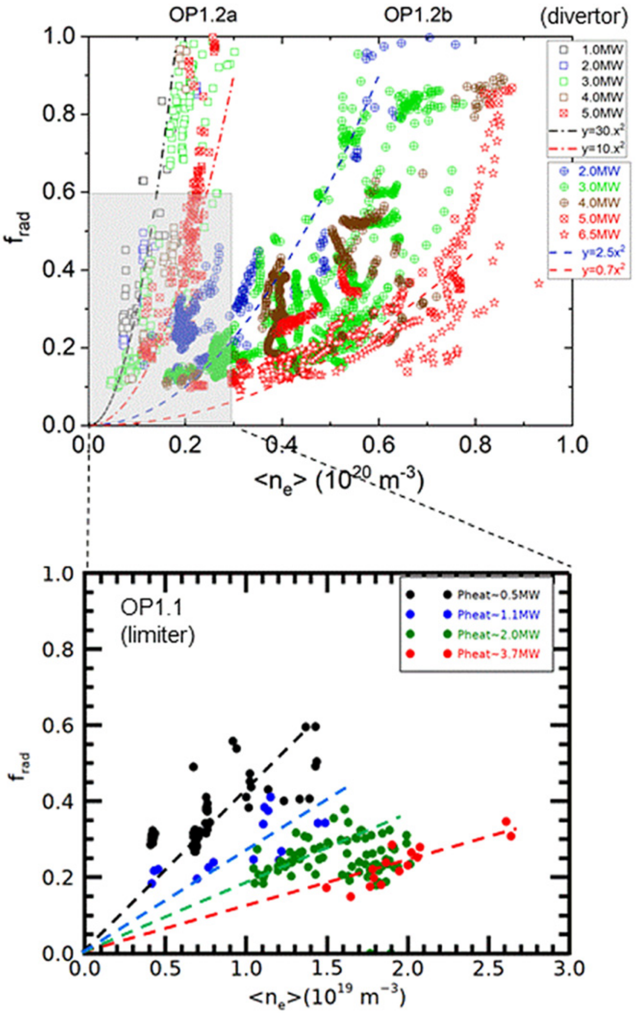

Figure 1. Summary of the radiation loss fraction, $f_{\rm rad}$, as a function of the average plasma density $\langle n_e \rangle$ during stationary phases (i.e. small variations in plasma energy within a time interval of about one energy confinement time) for divertor (OP1.2a,b; top) and limiter (OP1.1; bottom) configurations with varied $P_{\rm heat}$. Those for the divertor plasmas in the pre- and post-boronisation experiments fall into two branches because of the different impurity levels ($Z_{\rm eff} = 3.0$–4.5 for OP1.2a and 1.2–1.5 for OP1.2b). The fit functions, $y = kx^2$, are with varied k-values, which ranges from 10–30 for OP1.2a and 0.7–2.5 for post-boronization experiments in OP1.2b.

In general, a common feature of all the discharges studied here is that $f_{\rm rad}$ increases with plasma density for a fixed heating power, while for a fixed plasma density it decreases by increasing the heating power. Based on the relationship between the radiation power $P_{\rm rad}$ and the plasma density $\overline{n_e}$ as below [17],

$$P_{\rm rad} = V_{\rm p}\overline{n_e}^2 (Z_{\rm eff} - 1)\alpha_R, \tag{1}$$

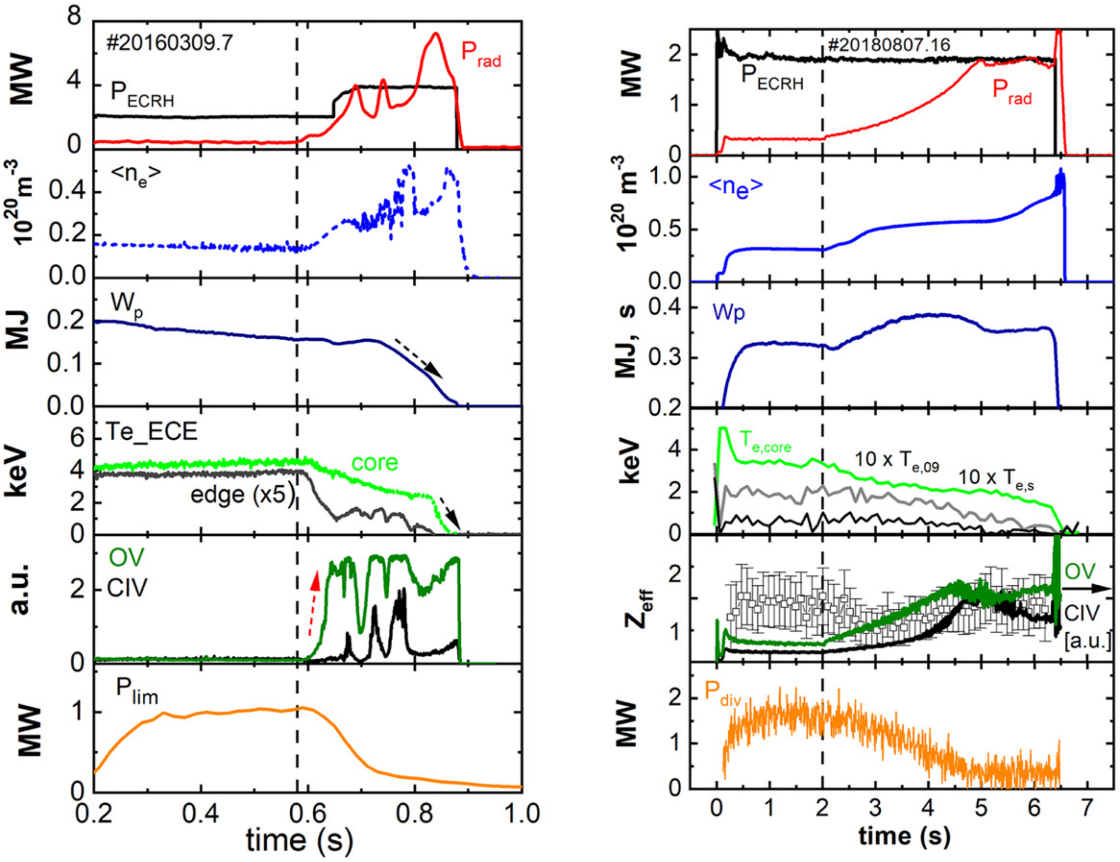

Figure 2. Time traces of plasma parameters in two representative discharges, XP20160309.7 (noted as XP7L) in the limiter configuration and XP20180807.16 (noted as XP16D) in the divertor 'standard' configuration. From top to bottom: ECR-heating power P_{ECRH} and total radiation power P_{rad}, line-averaged density $\langle n_{\mathrm{e}} \rangle$, plasma stored energy W_{P}, representative ECE channels for respective core and edge electron temperature T_{e}, the effective ion charge Z_{eff} (not available in XP7L), impurity line emission from CIV (154.8 nm) and OV (63.0 nm), and the total heat load on all divertor targets. Gas re-fueling is carried out at $t = 0.57$ s and 2.0 s for XP7L and XP16D, respectively (marked by the vertical dashed lines).

where V_{p} is the plasma volume, Z_{eff} the effective ion charge, and α_R is a function of temperature which is related to the heating power P_{heat}, the impurity species and their transport. Hence, f_{rad} can be expressed as $f_{\mathrm{rad}} = V_{\mathrm{p}}\overline{n_{\mathrm{e}}}^2(Z_{\mathrm{eff}} - 1)\alpha_f$, where $\alpha_f = \alpha_R/P_{\mathrm{heat}}$. According to the database in figure 1 (where $\langle n_{\mathrm{e}} \rangle$ has the same meaning as $\overline{n_{\mathrm{e}}}$), we obtain $\alpha_f \propto \mathrm{P_{heat}}^{-\beta}$ with β close to 1. The varied Z_{eff} value for OP1.2a ($Z_{\mathrm{eff}} = 3.0$–4.5) [12] and for OP1.2b ($Z_{\mathrm{eff}} = 1.2$–1.5) (see figure 2 (right)), which are derived from the spectroscopic bremsstrahlung measurements at W7-X [18], explains the separation of f_{rad} into two branches in figure 1 (top).

Figure 1 (bottom) demonstrates that most of the steady-state limiter plasmas have a radiation fraction $f_{\mathrm{rad}} < 45\%$ [16, 19, 20]. At higher radiation fractions, the limiter plasmas are usually unstable and thermal instabilities occur, causing a radiation collapse [16] (see an example in figure 2(*c*)). The plasma density up to $\langle n_{\mathrm{e}} \rangle \sim 2.5 \times 10^{19}$ m^{-3} is obtained for ECRH power up to ~4 MW. In contrast, most divertor plasmas can be operated stably at higher radiation levels up to $f_{\mathrm{rad}} \sim 0.9$–$1$ (with an uncertainty of 10%) without significant loss of energy content. Examples are presented in detail in the following section.

3. Beneficial effects of the island divertor vs limiter configuration

In general, the island divertor in W7-X has shown two beneficial effects in contrast with the limiter configuration concerning impurity radiation:

- Intensive radiation is located at the edge ($r/a > 0.8$) even at high radiation levels.
- The plasma remains stable up to a radiation fraction of ~0.9–1.0.

These are demonstrated using two comparative discharge examples. One is XP20160309.7 in OP1.1 (noted as XP7L henceforth) in a limiter configuration which is carried out shortly after daily wall-conditioning (glow-discharges in OP1.1) and should have a relatively low oxygen content. The other is XP20180807.16 in OP1.2b (noted as XP16D hereafter) in a divertor configuration which is a post-boronisation plasma also with a lower content of oxygen. Their time traces are shown in figure 2, left panels for XP7L and right panels for XP16D.

Both plasmas are generated with an ECRH power $P_{\mathrm{ECRH}} = 2$ MW, while in the later phase of XP7L ($t > 0.65$ s)

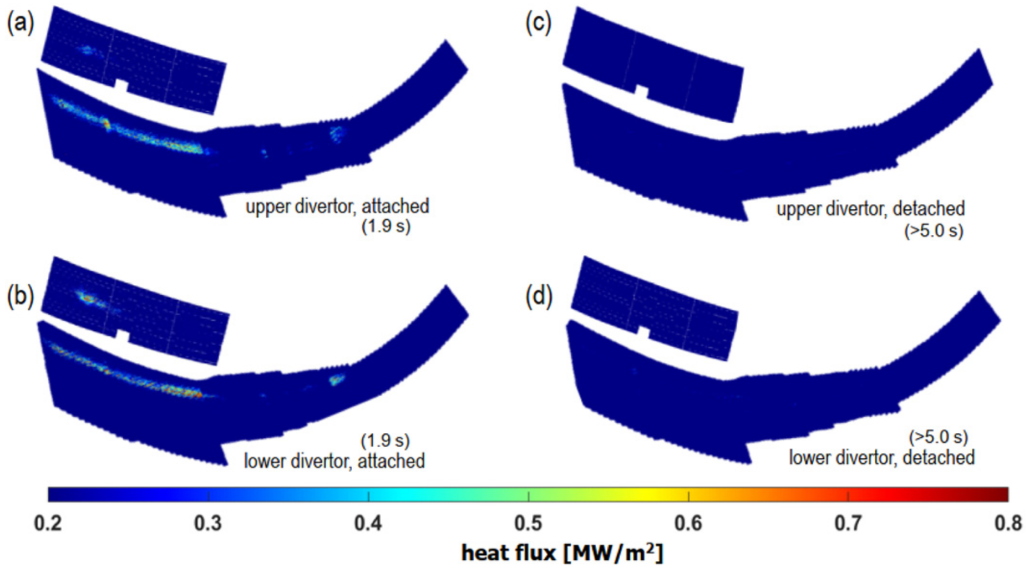

Figure 3. IR images of the (averaged) heat loads of the upper and lower divertor targets in XP16D for the attached plasma at $t = 1.9$ s in (*a*) and (*b*), respectively, and for the detached plasma phase at $t > 5.0$ s in (*c*) and (*d*), respectively, showing almost complete incoming-power-flux dissipation of the W7-X island divertor in high-density, high-radiation scenarios.

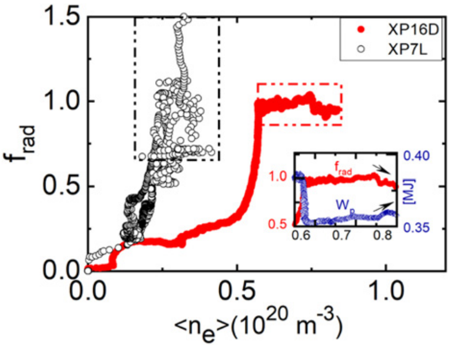

Figure 4. The evolution of the radiation loss fraction f_{rad} with plasma density in the limiter (XP7L) and divertor (XP16D) discharge. The black dashed-dotted rectangle marks the ranges with W_{p} drop in the limiter case and the red dashed-dotted range with f_{rad} ~ 1 (i.e. detached plasma) with ∼10% reduction of W_{p} in the diverter plasma (see the inset). For $\langle n_{\mathrm{e}}\rangle > 0.8 \times 10^{20}$ m^{-3}, f_{rad} decreases, corresponding to a decrease in carbon ion emission, as shown in figure 2 (right), accompanied by an increase in plasma energy W_{p}, as shown in the inset (indicated by the arrows).

it increases to 4 MW. Shortly after startup ($t = 0.5$ s), both plasmas have a radiation loss fraction f_{rad} ∼0.2 and a similar central electron temperature of $T_{\mathrm{e}}(0) \sim 4$ keV measured by the Thomson scattering [21, 22] for XP16D and ECE-diagnostic [23, 24] for XP7L. These diagnostics usually provide consistent results. The central ion temperature reaches ∼1.5 keV in both discharges (not shown in figure 2), which was measured with a multi-line x-ray imaging crystal spectrometer (XICS) in W7-X [25, 26]. The stored energy of the plasma W_{P}, measured with a compensated diamagnetic loop [27], reaches ∼0.2 MJ in XP7L; it increases by a factor of two in XP16D. The corresponding confinement time is ∼0.1 s and ∼0.2 s for XP7L and XP16D, respectively, which are close to the values (0.13 s and 0.25 s) obtained with ISS04 scaling [28] using the plasma minor radius $a = 49.\ 5$ cm, the rotational transform (at $r/a = 2/3$) $l_{2/3} = 0.83$, the plasma major radius $R = 5.5$ m, the averaged magnetic field strength $\langle B\rangle = 2.39$ T, $\langle n_{\mathrm{e}}\rangle = 1.7 \times 10^{19}$ m^{-3} for XP7L and $a = 51.\ 2$ cm, $l_{2/3} = 0.9$, $R = 5.5$ m, $\langle B\rangle = 2.41$ T, $\langle n_{\mathrm{e}}\rangle = 5.5 \times 10^{19}$ m^{-3} for XP16D, respectively. The experimental confinement time is at the level of 70–80% of scaling, which is typical for gas-fuelled discharges at relevant parameters [29].

In XP7L, the density decreases slightly (and so does the plasma energy W_{p}) for $t < 0.6$ s. After gas refueling at $t = 0.57$ s (marked by the vertical dashed line), the density $\langle n_{\mathrm{e}}\rangle$ increases accompanied by a rapid increase in P_{rad} following an obvious reduction of the heat load on the limiters, which is measured by IR-cameras [30]. The signal from the bolometer channels viewing $r/a \sim 0.8$ rapidly increase and show simultaneously an oscillation-like time evolution [31] (as does the edge temperature T_{e} (0.8) for $r/a = 0.8$ measured by ECE-diagnostic) while those viewing the outer plasma region detect reduced radiation, which indicates a radially inward movement of the radiation peak (see figure 4). The line emissions of the impurity ions, such as CIV (154.8 nm) and OV (63.0 nm), show also a similar behavior. The value of f_{rad} exceeds unity at $t > 0.8$ s, leading to a rapid decrease in both the core temperature and the plasma stored energy W_{p}.

In the case of the discharge XP16D, the gas refueling performed at $t = 2$ s (also marked by a vertical dashed line in figure 2 right) does not lead to the plasma instability described above. P_{rad} increases monotonically following the density rise (being consistent with the CIV (154.8 nm) and OV (63.0 nm) line emission) until f_{rad} reaches ∼1 at $t = 5$ s. The effective ion charge Z_{eff} varies during discharge and has a value of ∼1.5 for the low density and low radiation case ($t < 2$ s), which drops to ∼1.2 after gas refueling, but nears ∼1.5 in the high density and high radiation case. This phenomenon is believed to be related to the impurity transport at the W7-X SOL (see also section 4), which is associated with the variation of the magnetic island screening effect of impurities (depending on the edge plasma parameters (see figures 8(e) and (f)) [32]. The high f_{rad} value usually signifies a transitions of the plasma to a detached phase [12], which is confirmed by a significant reduction of the heat loads on the targets measured by nine IR cameras that provide almost 90% coverage of the divertor target plates [30, 33]. The time trace of the calculated total heat load on all the (ten) targets is shown in figure 2 (right; bottom). The 2D mapping of the averaged heat fluxes on the upper and lower divertor targets are shown in figures 3(*a*) and (*b*) for the attached plasma at $t = 1.9$ s and figures 3(*c*) and (*d*) for the detached plasma phase at $t > 5.0$ s, respectively. The peak heat flux reaches about 0.8 MW m^{-2} at $t = 1.9$ s with $f_{\mathrm{rad}} = 0.2$, which vanishes almost completely upon detachment (that is to a level of 0.2 MW m^{-2} corresponding to the camera resolution) at $t > 5.0$ s with $f_{\mathrm{rad}} \sim 1$. The IR images on the upper and lower targets in the attached plasma phase show differences possibly due to poloidal flows caused by $E_r \times B$ drift effects [34, 35].

In the later phase of the discharge ($t > 5.0$ s), $\langle n_{\mathrm{e}} \rangle$ rises steadily, which may lead to a further increase in P_{rad} followed by a decrease in W_{p} due to plasma energy depletion (when $P_{\mathrm{rad}} > P_{\mathrm{ECRH}}$). However, both P_{rad} and W_{p} maintains their high levels and the value W_{p} with only $\sim$10% reduction relative to its maximum ($\sim$0.38 MJ) until the end of the experimental program.

The evolution of f_{rad} with plasma density $\langle n_{\mathrm{e}} \rangle$ for both discharges are shown in figure 4. A rapid increase in f_{rad} occurs in both plasmas when the density reaches a critical value, which is $n_{\mathrm{e,c}} \sim 0.25 \times 10^{20}$ m^{-3} for XP7L and $n_{\mathrm{e,c}} \sim 0.6 \times 10^{20}$ m^{-3} for XP16D. However, the divertor plasma transitions to a quasi-stationary detached phase, while the limiter plasma experiences thermal instability (marked by a black dashed-dotted rectangle). The phases with $f_{\mathrm{rad}} > 1$ imply that the limiter plasma depletes the plasma energy W_{p} accompanied by a rapid decrease in $T_{\mathrm{e}}(0)$ (i.e. undergoing radiative collapse) as shown in figure 2 (left). In contrast, a stable W_{p} can be maintained in high-radiation scenarios up to f_{rad} approaching unity in the discharge XP16D in which a further increase in plasma density leads to a slight decrease in W_{p} ($\sim$10%) (marked by the red dashed-dotted rectangle). For $\langle n_{\mathrm{e}} \rangle > 0.8 \times 10^{20}$ m^{-3}, f_{rad} decreases, correlating with the decrease in C ion emission as shown by the CIV line emission in figure 2 (right) (those from other C-ions such as CIII, CII also behaves similarly). The O ion emission, represented by the OV line, remains almost unchanged, indicating that O impurities do not play a significant role here. The reduction in carbon ion emission is related to the impurity influx, impurity transport, as well as the Te- and ne-profile (see also figures 8(*e*) and (*f*)). Further investigations on carbon influx and transport studies connected to this phenomenon are ongoing. Details about the plasma radiation property are provided in the following sections.

4. Radiation intensity distributions

4.1. Comparisons between the limiter and divertor configuration

The 2D radiation distributions. The 2D radiation intensity distributions for selected time points in the discharges in figure 2 are obtained by bolometer tomography using the line-integrated measurements of the current bolometer system installed around the triangular plasma cross-section of W7-X [15]. In this cross section, the magnetic topology is symmetrical from top to bottom (i.e. up-down symmetry). The inversion algorithm based on reference [36] uses a new regularization functional based on relative gradient smoothing (RGS) of the sought emissivity profile. Details about the method can be found in reference [37]. The profile evolutions with density for both discharges are as follows:

- At the low-density, low-radiation phase for $t = 0.4$ s in XP7L and $t = 1.0$ s in XP16D, both plasmas are in quasi-stationary states with a similar line-averaged plasma density $\langle n_{\mathrm{e}} \rangle = 0.2$–$0.3 \times 10^{20}$ m^{-3} and $f_{\mathrm{rad}} \sim 0.2$. The corresponding 2D radiation distributions are shown in figures 5(*a*) and (*e*), respectively. A radiation zone that peaks at $r/a \sim 0.8$ within the LCFS of the limiter plasma is clearly visible, while in the divertor plasma it is displaced outward around the separatrix. Both the LCFS and the separatrix are shown in figure 5 with white lines. In both plasmas, more power is radiated from the plasma below the mid-plane, indicating an up-down asymmetry. An interesting but robust result is the 'double emission zone' that occurs in the divertor configuration and resides discretely inside and outside the confined plasma region. The inner zone generally shows a more uniformly distributed emissivity on the flux surfaces (FS) due to impurity ions of higher charged states (such as C4+ or O6+), while the outer zone shows a strong poloidal variation of emission due to lower-charged impurity ions. At this time point in XP16D, the plasma temperature close to the LCFS (at $r/a = 0.9$–1.0) is 50–150 eV (measured by the Thomson scattering system). We believe that the emissivity in the interior of the LCFS is associated with the intrusion of impurities and neutral hydrogen H_0. At this low density ($\sim 1.0 \times 10^{19}$ m^{-3} at the plasma edge), the neutral H_0 back-scatted from the divertor targets is energetic (with energy above several tens of eV) and has a long penetration length, and the magnetic islands show also a weaker screening effect on impurities [32], which are released from the targets by sputtering. Spectroscopic measurements show a higher Z_{eff} ($\sim$1.5) and the collected pulse height analysis (PHA) spectra [38] show a higher carbon concentration (not presented here) than that at medium density ($\sim$1.2; see figure 2 right), confirming a higher impurity content at such low density. Preliminary numerical simulations show that charge exchange between H_0 and impurity ions (cf also reference [39])

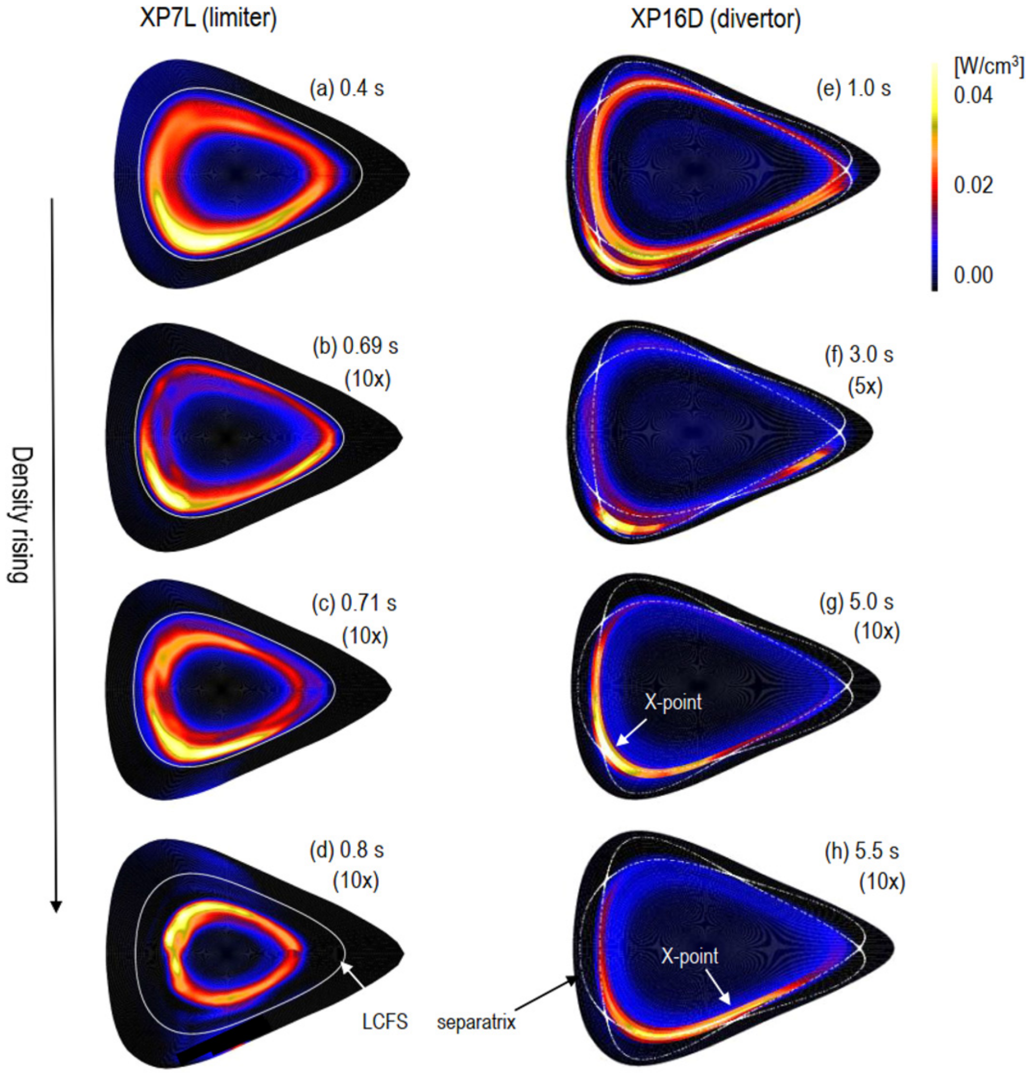

Figure 5. The 2D radiation distributions obtained from bolometer tomography for selected time points in the limiter plasma (XP7L) in (*a*)–(*d*) and divertor plasma (XP16D) in (*e*)–(*h*) show the evolution of the radiation zones and the poloidal asymmetry of the emissivity with plasma density. Also shown are the instability observed in the limiter plasma with reduced plasma volume during radiation collapse (*d*) and the intense radiation near *X*-points in the divertor plasma (*g*) and (*h*). The color bars for (*a*) and (*e*) are shown to the right of (*e*), while they are scaled by a factor of 5 for (*f*) and by a factor of 10 for the remaining panels.

further enhances emission of the highly ionized impurity within the LCFS. However, this issue will receive a further treatment in future work.

- At higher density after gas refueling, the limiter plasma shows instability and the radiation profile changes with time. The variations are exemplified in figure 5(*b*) for $t = 0.69$ s and figure 5(*c*) for $t = 0.71$ s. Both show an obviously enhanced up-down asymmetry while the latter shifts the entire radiation zone deeper inside the LCFS (see also the blue and green curves in figure 6(*a*)). In divertor discharge XP16D, with density rising, the local emissivity of the outer zone first increases, while that in the inner zone becomes relatively weaker (see figure 5(*f*)). The core radiation fraction $f_{\text{rad, core}}$, defined by $P_{\text{rad, core}}/P_{\text{rad}}$ with $P_{\text{rad, core}}$ representing the radiated power inside the LCFS, decreases accordingly (see also figure 7(*b*)). Further increasing $\langle n_{\text{e}} \rangle$ up to a critical density $n_{\text{e,c}}$, f_{rad} increases rapidly to unity following a transition to plasma detachment (at $t = 5.0$ s); the corresponding 2D radiation distribution is shown in figure 5(*g*). It is characterized by an intense radiation zone on the inboard side, especially around the lower inner *X*-point.
- Figure 5(d) shows the radiation profile in discharge XP7L while the plasma undergoes radiation collapse ($f_{\text{rad}} > 1$). The plasma shrinks significantly with a distinct 'flip' of the up-down asymmetry in the profile. For the discharge XP16D, we show in figure 5(*h*) the radiation distribution at $t = 5.5$ s with $\langle n_{\text{e}} \rangle = 0.62 \times 10^{20}$ m$^{-3} > n_{\text{e,c}}$ (in the region marked by the red rectangle in figure 4). The intense radiation zone shifts slightly radially inward and the maximum intensity is now around another *X*-point below the mid-plane, while that on the inboard side diminishes. Before the end of the discharge (at $t = 6.2$ s), the plasma density $\langle n_{\text{e}} \rangle$ is 0.8×10^{20} m^{-3}, exceeding the

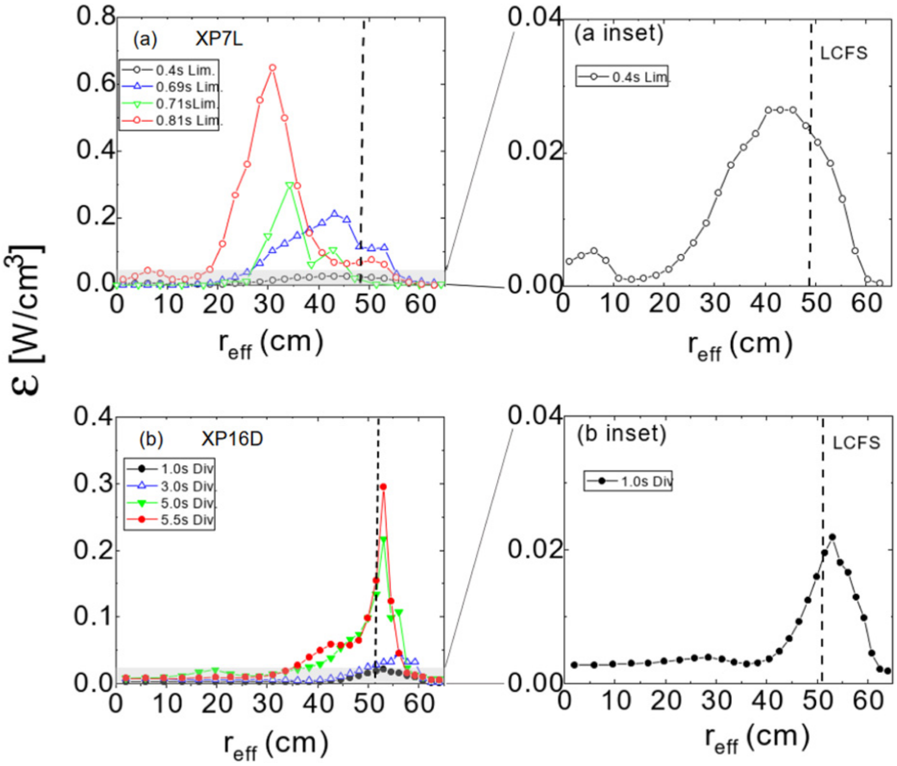

Figure 6. Comparisons of radial radiation profiles in the limiter plasma XP7L (*a*) and divertor plasma XP16D (*b*) in different radiation scenarios. Those in low-density, low-radiation scenarios (marked shaded) are expanded and shown on the right side to (*a*) and (*b*), respectively.

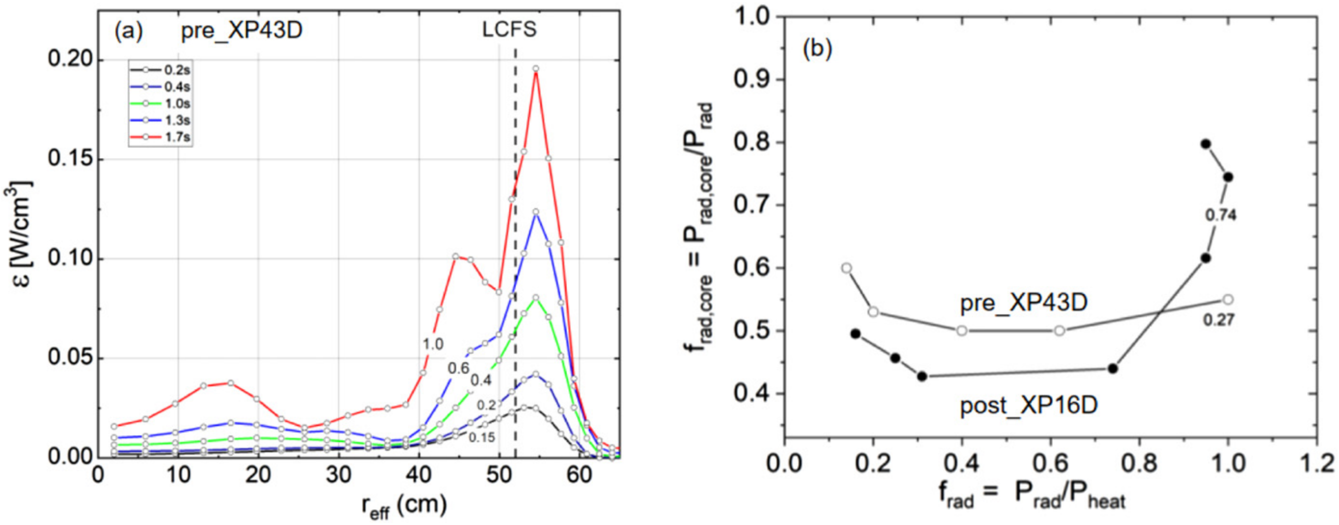

Figure 7. (*a*) Evolution of the radial 1D radiation profile with f_{rad} derived from 2D tomographic reconstructions using bolometer measurements in the selected pre-boronisation discharge XP20171108.43 (labeled 'pre_XP43D'). The values of f_{rad} are marked in the curves; (*b*) Comparisons of the fraction of radiated power from the confined plasma region, $f_{\mathrm{rad,\,core}}$, between two representative discharges in OP1.2a before boronisation (XP20171108.43 labeled 'pre_XP43D') and in OP1.2b after boronisation (XP20180807.16 labeled 'post_XP16D'). The values marked in the curves are the plasma density in [10^{20} m^{-3}] for $f_{\mathrm{rad}} \sim 1$.

critical density $n_{\mathrm{e,c}} = 0.6 \times 10^{20}$ m^{-3} for the detachment transition by a factor of 1.3, but W_{p} maintains its level; Decrease in f_{rad} is visible and is consistent with the reduction in CIV line emission, as shown in figure 2 (right). This phenomenon is believed to be related to impurity transport, as both the density and temperature profiles at $t = 6.2$ s (see figures 8(*e*) and (*f*)) vary relative to those at $t = 5.0$ s (immediately after the detachment transition). Further studies are required.

The radial 1D radiation profiles. Figures 6(*a*) and (*b*) demonstrate the radial 1D radiation profiles obtained by poloidal averaging over the 2D profiles shown in figures 5(*a*)–(*h*) for limiter plasma XP7L and divertor plasma XP16D, respectively. The vertical dashed line represents the radial positions of the LCFS for both the limiter and divertor configurations. They show that, at low-density, low-f_{rad} case, the limiter plasma has an emission peak about 10 cm inside the LCFS, whereas the divertor plasma has an emission peak much closer to the LCFS. The emissivity in this scenario has a peak value of $\varepsilon_{\mathrm{m}} \sim 0.03$ W cm^{-3}, which is more than 10 times weaker than that in the high-radiation scenario (see the shaded area). For clarity, the profiles at the low-f_{rad} cases in XP7L and XP16D are illustrated in magnification on the right to figures 6(*a*) and (*b*), respectively.

The narrow peak profiles, especially for the high f_{rad} scenarios (e.g. at $t = 5$ s in figure 6(*b*)), characterize the substantial carbon emission after wall boronisation in W7-X. Examples from the experiments before boronisation are shown in the following section for a comparison. The radial inward shift of the radiation peak for the high radiation phase (in red) is distinct compared to the cases for the low radiation scenario (in blue) for both discharges. However, they lead to different plasma stability, one leading to thermal collapse in the limiter discharge and the other to a quasi-stable detached divertor plasma. Here, the radial position of the radiation peak plays a significant role.

It is noteworthy that the up-down asymmetry in the radiation pattern is sustained for all plasma phases studied and its magnitude increases with the radiation level. In experiments with reversed magnetic field direction, a 'reversal' of the asymmetry is observed, suggesting that particle flux-friction relationship plays a role here. Details can be found in reference [37].

4.2. Comparisons between discharges in pre- and post-boronisation experiments

The wall boronisation performed in OP1.2b markedly reduces the carbon and oxygen yields in W7-X [40–42]. Before boronisation in OP1.2a, oxygen impurity radiation usually dominates the total impurity radiation based on the fact that P_{rad} is strongly correlated with OVI line emission [12]. Nevertheless, the impurity radiation in discharges before boronisation behaves quite similarly to that in experiments after boronisation, such as edge localization of the radiation zone and visible up-down asymmetry. Yet, they differ in the following respects:

(a) In the low-density scenario, the 'double emission zone' in the OP1.2b plasma, as shown in figure 5(*e*), smears into one [37].
(b) The radiation profiles in OP1.2a (before boronisation) are generally broader around the LCFS than those in the discharges after boronisation.
(c) The threshold density $n_{\mathrm{e,c}}$ for f_{rad} approaching unity (i.e. detachment transition) is lower by a factor ∼3.

Figure 7(*a*) shows the evolution of the radial emissivity profile with increasing density in a typical pre-boronisation experiment in 'standard' configuration (XP20171108.43) with 3 MW ECRH power. At the selected time points, the plasma density increases from 0.6 to 2.7×10^{19} m^{-3} and f_{rad} increases correspondingly from 0.15 to ∼1.0. All the profiles shown have peaks outside the LCFS. A second peak inside the LCFS gradually emerges at $r_{\mathrm{eff}} \sim 45$ cm and becomes pronounced for $f_{\mathrm{rad}} \sim 1$ (in red), which is related to highly charged impurity ions (such as O6+, C4+). The radiated power loss from the confined plasma region varies with the profile shape following the increase of the radiation level. The factor $f_{\mathrm{rad,\,core}} = P_{\mathrm{rad,\,core}}/P_{\mathrm{rad}}$, is derived from the radiation profiles, which has an uncertainty of ∼15%. It is observed that the lowest $f_{\mathrm{rad,\,core}}$ is ∼0.5 occurring at intermediate f_{rad} (∼50%). In low and high radiation scenarios, it can reach ∼60%. This is shown in figure 6(*b*) (in open circles).

In post-boronisation discharges, the lowest value of $f_{\mathrm{rad,\,core}}$ becomes lower (∼40%) due to lower impurity content. Nevertheless, it reaches 50% in the low-f_{rad} case and increases to ∼60% for the case f_{rad} approaching unity. For deeply detached plasmas ($n_{\mathrm{e}} > n_{\mathrm{e,c}}$), this factor can even reach ∼80%. These observations are shown in figure 6(*b*) (in solid circles) taking XP20180807.16 (the same as shown in figure 2) as example. The values marked in the curves are the corresponding values of $n_{\mathrm{e,c}}$ in [10^{20} m^{-3}] for transition to $f_{\mathrm{rad}} \sim 1$. It is also observed that the level of $f_{\mathrm{rad,\,core}}$ is correlated to some extent with the Z_{eff} value (see figure 2 in section 3).

5. Discussions and summary

In W7-X, the impurity radiation usually limits the maximum achievable plasma density [16, 43]. In the limiter configuration, the radiation zones are ∼10 cm inside the confined plasma region and almost all of the radiated power comes from the confined plasma region (>90%). With the exception of the low-power heated plasma, quasi-stationary operation for the limiter plasma is only achievable for $f_{\mathrm{rad}} < 45\%$. For higher radiation fractions, thermal instability occurs. This is attributed to direct contamination of the core plasma by enhanced impurity sources [44–46] and/or inward transport of impurities from the limiters. In contrast, impurities released due to plasma surface interaction in the divertor configuration [47] radiate in

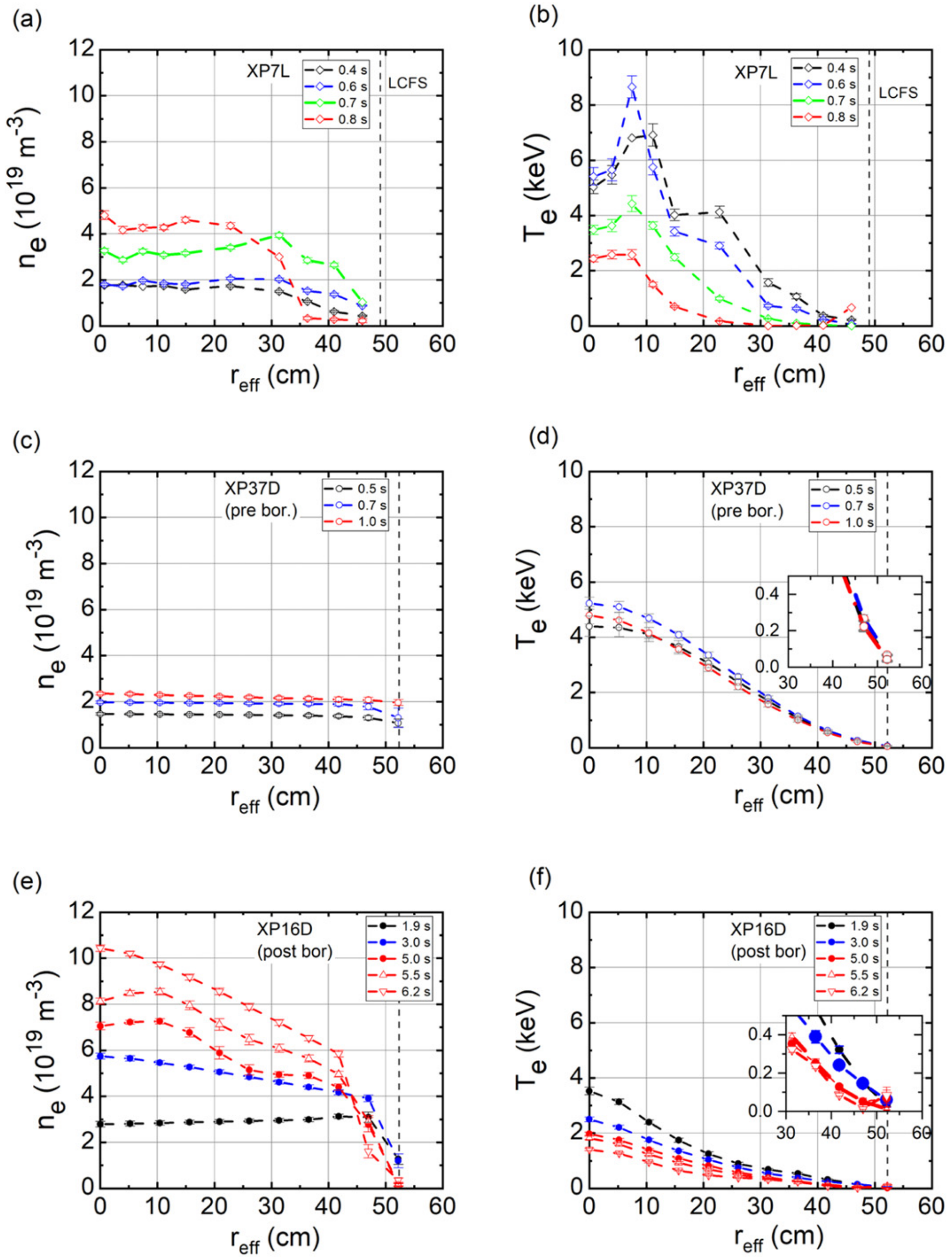

Figure 8. Comparisons of density and temperature profiles measured by Thomson scattering for different plasma radiation scenarios in the limiter plasma XP7L, the plasma before wall boronisation XP20171109.37 (denoted as XP37D representing XP43D in figure 7 due to lack of Thomson scattering data there) and that after boronisation XP16D. All red symbols represent plasma parameters in scenarios with a high radiation level (f_{rad} ∼0.9–1.0), while the black symbols represent cases with low f_{rad} (30%–40%). The T_e values in the outer plasma region for XP37D and XP16D are shown in the inset in (*d*) and (*f*) for displaying their variations. The vertical dashed lines indicate the radial position of the LCFS.

the plasma periphery ($r/a > 0.8$) around the LCFS. As the plasma density increases, the radiated power fraction within the LCFS can vary depending on the radiation loss fraction, which is associated with impurity transport and plasma parameters at the edge, and the plasma can maintain its stability. This is observed in both divertor plasmas before and after wall boronisation.

After boronisation, the plasma densities required to access high radiation regimes increase by a factor of ∼3 (see figures 1 and 6(*b*)), and the radiation distribution localized at the plasma edge becomes more peaked.

The presented properties of W7-X plasma radiation strongly depend on the magnetic configuration, impurity species/source (associated with wall conditioning), and the background plasma parameters that affect impurity transport. The density and temperature profiles measured by Thomson scattering for different plasma radiation scenarios in the studied plasma are summarized in figure 8. In the absence of Thomson scattering data of XP43D (see figure 7), we take XP20171109.37 (denoted as XP37D) as a proxy, since the plasma is also obtained with the 3 MW ECRH as in XP43D. The temperature profiles of the ions are not shown because in the outer confined plasma region where the radiation zone is located, the values of T_i and T_e are close to each other.

It can be seen that (1) in the low-f_rad cases (the black open or filled circles) the strongest radiation (at $r/a = 0.8$, see figure 6(*a*) (inset)) in the limiter plasma XP7L occurs with T_e ~350 eV and $n_\mathrm{e} = 0.6 \times 10^{19}$ m^{-3}, while it in the divertor plasma (in the SOL with $r/a > 1$) occurs with $T_\mathrm{e} < 100$ eV for XP37D before boronization and also for XP16D after boronization. The plasma density in the SOL is less than 1.0–2.0 × 10^{19} m^{-3} for the plasma studied, as recorded by electric probes mounted on a reciprocating manipulator close to the outboard mid-plane [48–50]. 2) As $\langle n_\mathrm{e}\rangle$ increases, the overall density profile normally increases (accompanied by a decrease in the T_e profile); Reaching a critical value of $\langle n_\mathrm{e}\rangle$, the limiter plasma becomes thermally unstable undergoing radiative collapse (see the contracted n_e and T_e profiles in figures 8(*a*) and (*b*) (in red)) and the divertor plasma transitions to high radiation scenarios. This critical density is dependent on the heating power and the impurity content (see also figure 1). It is noteworthy that the evolution of the density profile in XP16D after boronization differs from that in XP37D: (a) in XP16D, the edge plasma density (at $r/a = 0.9$) reaches 4.0×10^{19} m^{-3} at intermediate f_rad ($t = 3.0$ s; blue circles), which is higher than that in the high density and high radiation cases (red symbols in figure 8(*e*)). The SOL plasma density in the high-f_rad cases is not available in the plasma studied, but its decrease has been detected by the electric probes in other discharges under similar plasma conditions. The relative decrease in the SOL plasma density is associated with the decrease in ionization of the recycled neutral hydrogen due to the lower power entering the SOL in high radiation scenarios [50]. (b) In XP16D, central peak density profiles appear, especially pronounced in the deeply detached plasma phase (see figure 8(*e*) for $t = 6.2$ s) in red), while in XP37D the plasma density profiles remain flat (see figure 8(*c*)).

Numerical simulations of the impurity radiation profiles based on 1D impurity transport model are being initialized, but face challenges because the plasma parameters around the LCFS are subject to large uncertainties. More accurate simulations of the W7-X plasma radiation require actually 3D modeling. However, the current version of the EMC3-Eirene code (without drifts) for 3D modeling is not yet able to quantitatively reproduce all selected local measurements simultaneously under the current experimental conditions (in particular, the existence of error fields) [52]. Some results using EMC3-Eirene code are reported in [37, 51] and comparisons with the bolometer results (in OP1.2a before boronisation) show qualitative agreements but also differences, especially in the asymmetric feature of the impurity radiation distribution.

Here we have reported that poloidal asymmetries in the radiation distribution have been observed for both limiter and divertor plasmas (after boronization). Similar to the description in reference [37], the magnitude of the asymmetry increases toward the high density, high radiation scenarios. This asymmetry reverses under certain plasma conditions, e.g. when the magnetic field direction is reversed or when the plasma dimension becomes smaller, as shown in figure 4 for the limiter plasma (a similar phenomenon has also been observed for divertor plasmas). Detail studies and discussions about the underlying physics can be found in [37].

The plasma in the divertor configuration can maintain stability at high radiation level with f_rad approaching unity. Moreover, the stability retains when the density becomes somewhat higher (up to a factor of 1.3) than the threshold density after detachment transition. In this case, the edge plasma temperature decreases in response to the density increase (see $t > 5$ s in figure 2 right). As a result, the radiation zone shifts radially inward (see figure 4(*h*), which follows an increase in $f_\mathrm{rad,\,core}$ and leads to a small reduction in stored energy (10%–15%). This phenomenon demonstrates the self-regulating capability of the W7-X divertor plasma, which is qualitatively consistent with the recent simulation results using the EMC3-Eirene code [52]. However, the asymmetric radiation feature obtained with bolometer tomography (figure 4) differs from the simulation results.

As described, the island divertor concept at W7-X provides a large operating window up to high-density, high-radiation scenarios compared to the limiter configuration, and is already showing its beneficial effects in terms of power removal capability due to impurity radiation [12, 13]. However, a deeper understanding of the experimental observations, such as the asymmetry in the radiation distribution and its influence on the edge plasma parameters as well as the plasma performance, requires further investigation.

Acknowledgments

One of the authors thanks Mr. M Marquardt and Dr. A Werner for support in DAQ and Dr. C Killer for providing information on the plasma parameters of W7-X SOL. This work has been carried out within the framework of the EUROfusion Consortium and has received funding from the Euratom research and training programme 2014–2018 and 2019–2020 under Grant Agreement No. 633053. The views and opinions expressed herein do not necessarily reflect those of the European Commission. This work was supported by the U.S. Department of Energy (DoE) under Grants Nos. DE-AC02-09CH11466 and DE-SC0014210.

ORCID iDs

D. Zhang https://orcid.org/0000-0002-5800-4907
Y. Feng https://orcid.org/0000-0002-3846-4279
B. Buttenschön https://orcid.org/0000-0002-9830-9641
C.D. Beidler https://orcid.org/0000-0002-4395-239X
L. Giannone https://orcid.org/0000-0001-5611-200X
A. Pavone https://orcid.org/0000-0003-2398-966X
M. Beurskens https://orcid.org/0000-0002-3354-0279
S. Bozhenkov https://orcid.org/0000-0003-4289-3532
J.K. Brunner https://orcid.org/0000-0002-0974-0457
F. Effenberg https://orcid.org/0000-0002-4846-4598
Y. Gao https://orcid.org/0000-0001-8576-0970
J. Geiger https://orcid.org/0000-0003-4268-7480
M. Jakubowski https://orcid.org/0000-0002-6557-3497
S. Kwak https://orcid.org/0000-0001-7874-7575
H. Niemann https://orcid.org/0000-0003-0300-1060
T. Sunn Pedersen https://orcid.org/0000-0002-9720-1276
N. Pablant https://orcid.org/0000-0001-6617-8459
K. Rahbarnia https://orcid.org/0000-0002-5550-1801
P. Drews https://orcid.org/0000-0002-6567-1601
G. Weir https://orcid.org/0000-0002-2370-409X
V. Winters https://orcid.org/0000-0001-8108-7774

References

[1] Nührenberg J. 2010 Development of quasi-isodynamic stellarators *Plasma Phys. Control. Fusion* **52** 124003

[2] Renner H., Boscary J., Greuner H., Grote H., Hoffmann F.W., Kisslinger J., Strumberger E. and Mendelevitch B. 2002 Divertor concept for the W7-X stellarator and mode of operation *Plasma Phys. Control. Fusion* **44** 1005

[3] Sunn Pedersen T. *et al* 2015 Plans for the first plasma operation of Wendelstein 7-X *Nucl. Fusion* **55** 126001

[4] Wolf R.C., Beidler C.D., Dinklage A., Helander P., Laqua H.P., Schauer F., Sunn Pedersen T. and Warmer F. 2016 Wendelstein 7-X program-demonstration of a stellarator option for fusion energy *IEEE Trans. Plasma Sci.* **44** 1466–71

[5] Klinger T. *et al* 2016 Performance and properties of the first plasmas of Wendelstein 7-X *Plasma Phys. Control. Fusion* **59** 014018

[6] Dinklage A. *et al* 2018 Magnetic configuration effects on the Wendelstein 7-X stellarator *Nat. Phys.* **14** 855–60

[7] Klinger T. *et al* 2019 Overview of first Wendelstein 7-X high-performance operation *Nucl. Fusion* **59** 112004

[8] Pedersen T.S. *et al* 2019 First divertor physics studies in Wendelstein 7-X *Nucl. fusion* **59** 096014

[9] Effenberg F. *et al* 2017 Numerical investigation of plasma edge transport and limiter heat fluxes in Wendelstein 7-X startup plasmas with EMC3-EIRENE *Nucl. Fusion* **57** 036021

[10] Bozhenkov S.A. *et al* 2017 Effect of error field correction coils on W7-X limiter loads *Nucl. Fusion* **57** 126030

[11] Geiger J., Beidler C.D., Feng Y., Maaßberg H., Marushchenko N.B. and Turkin Y. 2014 Physics in the magnetic configuration space of W7-X *Plasma Phys. Control. Fusion* **57** 014004

[12] Zhang D. *et al* 2019 First observation of a stable highly dissipative divertor plasma regime on the Wendelstein 7-X stellarator *Phys. Rev. Lett.* **123** 025002

[13] Schmitz O. *et al* 2020 Stable heat and particle flux detachment with efficient particle exhaust in the island divertor of Wendelstein 7-X *Nucl. Fusion* **61** 016026

[14] Laqua H. *et al* 2019 Overview of W7-X ECRH results 203 *EPJ Web of Conf.* (EDP Sciences)

[15] Zhang D. *et al* 2010 Design criteria of the bolometer diagnostic for steady-state operation of the W7-X stellarator *Rev. Sci. Instrum.* **81** 10E134

[16] Zhang D. *et al* 2017 The bolometer diagnostic at Wendelstein 7-X and its first results from the initial campaign *Stellarator News* Issue 157

[17] Roberts D.E. 1981 Total impurity radiation power losses from steady-state tokamak plasmas *Nucl. Fusion* **21** 215

[18] Pavone A. *et al* 2019 Measurements of visible bremsstrahlung and automatic Bayesian inference of the effective plasma charge Z_{eff} at W7-X *J. Instrum.* **14** C10003

[19] Hirsch M. *et al* 2017 Confinement in Wendelstein 7-X limiter plasmas *Nucl. Fusion* **57** 086010

[20] Fuchert G. *et al* 2018 Global energy confinement in the initial limiter configuration of Wendelstein 7-X *Nucl. Fusion* **58** 106029

[21] Pasch E., Beurskens M.N.A., Bozhenkov S.A., Fuchert G., Knauer J. and Wolf R.C. 2016 The Thomson scattering system at Wendelstein 7-X *Rev. Sci. Instrum.* **87** 11E729

[22] Bozhenkov S.A. *et al* 2017 The Thomson scattering diagnostic at Wendelstein 7-X and its performance in the first operation phase *J. Instrum.* **12** P10004

[23] Hirsch M. *et al* 2019 ECE diagnostic for the initial operation of Wendelstein 7-X 203 *EPJ Web of Conferences* (EDP Sciences)

[24] Hoefel U. *et al* 2019 Bayesian modeling of microwave radiometer calibration on the example of the Wendelstein 7-X electron cyclotron emission diagnostic *Rev. Sci. Instrum.* **90** 043502

[25] Pablant N.A. *et al* 2018 Core radial electric field and transport in Wendelstein 7-X plasmas *Phys. Plasmas* **25** 022508

[26] Langenberg A. *et al* 2018 Prospects of X-ray imaging spectrometers for impurity transport: recent results from the stellarator Wendelstein 7-X (invited) *Rev. Sci. Instrum.* **89** 10G101

[27] Rahbarnia K. *et al* 2018 Diamagnetic energy measurement during the first operational phase at the Wendelstein 7-X stellarator *Nucl. Fusion* **58** 096010

[28] Yamada H. *et al* 2005 Characterization of energy confinement in net-current free plasmas using the extended international stellarator database *Nucl. Fusion* **45** 1684

[29] Fuchert G. *et al* 2020 Increasing the density in Wendelstein 7-X: benefits and limitations *Nucl. Fusion* **60** 036020

[30] Jakubowski M. *et al* 2018 Infrared imaging systems for wall protection in the W7-X stellarator (invited) *Rev. Sci. Instrum.* **89** 10E116

[31] Zhang D. *et al* 2016 Investigation of the radiative power loss in the limiter plasmas of W7-X *43rd EPS Conf. Plasma Physics* (https://kuleuvencongres.be/eps2016) (Leuven, Belgium, 4-8 July 2016) (European Physical Society)

[32] Feng Y., Kobayashi M., Lunt T. and Reiter D. 2011 Comparison between stellarator and tokamak divertor transport *Plasma Phys. Control. Fusion* **53** 024009

[33] Gao Y., Jakubowski M.W., Drewelow P., Pisano F., Puig Sitjes A., Niemann H., Ali A. and Cannas B. 2019 Methods for quantitative study of divertor heat loads on W7-X *Nucl. Fusion* **59** 066007

[34] Feng Y., Herre G., Grigull P. and Sardei F. 1998 The effects of field reversal on the W7-AS island divertor at low densities *Plasma Phys. Control. Fusion* **40** 371

[35] Hammond K.C. *et al* 2019 Drift effects on W7-X divertor heat and particle fluxes *Plasma Phys. Control. Fusion* **61** 125001

[36] Anton M., Weisen H., Dutch M.J., von der Linden W., Buhlmann F., Chavan R., Marletaz B., Marmillod P. and Paris

P. 1996 X-ray tomography on the TCV tokamak *Plasma Phys. Control. Fusion* **38** 1849

[37] Zhang D. *et al* 2021 Bolometer Tomography on Wendelstein 7-X for Study of Radiation Asymmetry *Nucl. Fusion* **61** 116043

[38] Jabłoński S. *et al* 2015 Simulation of pulse height analysis soft X-ray spectra expected from W7-X *J. Instrum.* **10** P10021

[39] McCarthy K.J., Zurro B., Burgos C., Vega J. and Portas A. 1995 Investigation of Cv line ratio variations in a tokamak with an application to neutral hydrogen measurement *Phys. Rev.* E **52** 6671

[40] Brakel R. *et al* 2018 Strategy and optimisation of wall conditioning at the Wendelstein 7-X stellarator *27th IAEA Fusion Energy Conf.* (Gandhinagar) (https://www.iaea.org/events/fec-2018))

[41] Wauters T. *et al* 2020 Wall conditioning in fusion devices with superconducting coils *Plasma Phys. Control. Fusion* **62** 034002

[42] Sereda S. *et al* 2020 Impact of boronizations on impurity sources and performance in Wendelstein 7-X *Nucl. Fusion* **60** 086007

[43] Fuchert G., Brunner K. and Rahbarnia K. (W7-X-Team) 2018 Increasing the density in W7-X: benefits and limitations

[44] Wauters T. *et al* 2018 Wall conditioning by ECRH discharges and He-GDC in the limiter phase of Wendelstein 7-X *Nucl. Fusion* **58** 066013

[45] Winters V.R. *et al* 2017 Overview of the plasma-surface interaction on limiter surfaces in the startup campaign of Wendelstein 7-X *Phys. Scr.* T **170** 014050

[46] Wurden G.A. *et al* 2017 Limiter observations during W7-X first plasmas *Nucl. Fusion* **57** 056036

[47] Wang E. *et al* 2020 Impurity sources and fluxes in W7-X: from the plasma-facing components to the edge layer *Phys. Scr.* T **171** 014040

[48] Killer C. *et al* 2019 Characterization of the W7-X scrape-off layer using reciprocating probes *Nucl. Fusion* **59** 086013

[49] Drews P. *et al* 2017 Measurement of the plasma edge profiles using the combined probe on W7-X *Nucl. Fusion* **57** 126020

[50] Drews P. *et al* 2019 Edge plasma measurements on the OP 1.2a divertor plasmas at W7-X using the combined probe *Nucl. Mater. Energy* **19** 179–83

[51] Feng Y. *et al* 2021 Understanding detachment of the W7-X island divertor *Nucl. Fusion* **61** 086012

[52] Feng Y. *et al* 2021 First attempt to quantify W7-X island divertor plasma by local experiment-model comparison *Nucl. Fusion* **61** 106018